ADVANCED MATERIALS
www.advmat.de

Gradient Doping in Sn–Pb Perovskites by Barium Ions for Efficient Single-Junction and Tandem Solar Cells

*Zhenhua Yu, Xihan Chen, Steven P. Harvey, Zhenyi Ni, Bo Chen, Shangshang Chen, Canglang Yao, Xun Xiao, Shuang Xu, Guang Yang, Yanfa Yan, Joseph J. Berry, Matthew C. Beard, and Jinsong Huang**

Narrow-bandgap (NBG) tin (Sn)–lead (Pb) perovskites generally have a high density of unintentional p-type self-doping, which reduces the charge-carrier lifetimes, diffusion lengths, and device efficiencies. Here, a p–n homojunction across the Sn–Pb perovskite is demonstrated, which results from a gradient doping by barium ions (Ba^{2+}). It is reported that 0.1 mol% Ba^{2+} can effectively compensate the p-doping of Sn–Pb perovskites or even turns it to n-type without changing its bandgap. Ba^{2+} cations are found to stay at the interstitial sites and work as shallow electron donor. In addition, Ba^{2+} cations show a unique heterogeneous distribution in perovskite film. Most of the barium ions stay in the top 600 nm region of the perovskite films and turn it into weakly n-type, while the bottom portion of the film remains as p-type. The gradient doping forms a homojunction from top to bottom of the perovskite films with a built-in field that facilitates extraction of photogenerated carriers, resulting in an increased carrier extraction length. This strategy enhances the efficiency of Sn–Pb perovskite single-junction solar cells to over 21.0% and boosts the efficiencies of monolithic perovskite–perovskite tandem solar cells to 25.3% and 24.1%, for active areas of 5.9 mm^2 and 0.94 cm^2, respectively.

1. Introduction

With a rapid increase in power conversion efficiency (PCE) from ≈3.8% to 25.7% in the last few years,[1–7] metal halide perovskites (MHP) have emerged as emerging materials in photovoltaic (PV) technologies. While most of the research efforts have focused on lead (Pb)-based MHP single junction PV cells, MHP-based tandem solar cells fabricated by combining MHP layers with silicon, Cu(In, Ga)Se_2 (CIGS), or another low-bandgap MHP are gaining increasing attention because of their potential to overcome the detailed balance limit of single junction PV cells and thus leading to a further reduction in the cost of PV technologies.[8–12] Among these technologies, MHP–MHP tandem cells can be fabricated employing all solution-based processes to retain the low-fabrication cost merit yet still retain high PCEs and flexible.[13,14] Narrow-bandgap (NBG) tin (Sn)–Pb perovskites can reach a lowest bandgap of 1.21 eV with a Sn/Pb ratio of ≈1, which paired with a wide-bandgap (WBG) MHP with a bandgap of 1.80 eV can reach a maximum efficiency of over 30%.[14,13]

As a crucial part of MHP–MHP tandem cells, the Sn–Pb NBG perovskite single-junction solar cells still have low PCEs compared to their bandgap entitlement in order realize the full potential of tandem structures.[7,14,15] The best certified PCE for a Sn–Pb NBG single junction solar cells to date is 20.7%,[16] which is much lower than that of silicon or CIGS single junction cells. There are still several obstacles for further improvement of Sn–Pb perovskite, such as low absorption coefficient[17] prone to be oxidized,[18] poor thermal[19] stability, high self p-doping,[17,20] and relatively short carrier diffusion length.[17] Due to the relatively smaller absorption coefficient compared to Pb perovskites, Sn–Pb NBG absorbers must be at least 1 µm thick to ensure efficient light absorption, and a commensurate increase of the minority-carrier diffusion lengths into the several µm range are needed to ensure efficient charge collection. The most outstanding challenge limiting long carrier diffusion lengths in Sn–Pb NBG perovskites is reportedly the presence of a high density of residual p-type carriers.[17,20] The p-type self-doping is known to be induced by Sn vacancies which generally pair with Sn^{4+} to maintain charge neutrality.[21–23] Sn^{2+} is thermodynamically instable for the low oxidation potential of E_O = 0.15 V for Sn^{2+}/Sn^{4+}.[23–25] Therefore, Sn vacancies are prone to form upon oxidation of Sn^{2+} to Sn^{4+} which can occur during any step of the device construction from raw materials up to encapsulated Sn–Pb perovskite-based

Z. Yu, Z. Ni, B. Chen, S. Chen, X. Xiao, S. Xu, G. Yang, J. Huang
Department of Applied Physical Sciences
University of North Carolina
Chapel Hill, NC 27599, USA
E-mail: jhuang@unc.edu
X. Chen, S. P. Harvey, J. J. Berry, M. C. Beard
National Renewable Energy Lab
Golden, CO 80401, USA
X. Chen
Department of Mechanical and Energy Engineering
Southern University of Science and Technology
Shenzhen, Guangdong 518055, China
C. Yao, Y. Yan
Department of Physics and Astronomy
University of Toledo
Toledo, OH 43606, USA
The ORCID identification number(s) for the author(s) of this article can be found under https://doi.org/10.1002/adma.202110351.

DOI: 10.1002/adma.202110351

devices. Adding reductants or antioxidants into the Sn–Pb perovskite precursors were reported to suppress Sn vacancy formation, which increased the carrier diffusion length.[20,26] 2D materials on the surface and at the grain boundaries were also applied to enhance the carrier diffusion length by suppressing p-type defect formation.[27,28] However, Sn–Pb perovskites treated by the all existing methods still exhibit a hole concentration of 5×10^{15} cm^{-3} or more,[20,29] which is relatively high in comparison to pure Pb-based MHP solar cells of $\approx 3 \times 10^{14}$ cm^{-3}.[30,31] This indicates Sn vacancies are formed during the perovskite film formation process which are not effectively suppressed by using these antioxidant approaches. Therefore, additional strategies are needed to suppress excess hole formation and effectively decrease the p-doping of Sn–Pb perovskites to further enhance their device efficiency.

Here, we report that the addition of a small amount (0.1 mol% to Pb) of barium iodide (BaI_2) into the precursor solution can effectively compensate the p-doping of Sn–Pb NBG perovskites. We discovered that divalent metal cations such as Ba^{2+} decreases the hole density Sn–Pb perovskites and can convert the film into weakly n-type. An inhomogeneous distribution of Ba^{2+} cations in Sn–Pb perovskite films along the out-of-plane direction is induced by the unique film formation process and thus generates a p–n homojunction. This combination of effects contributed to the reduction of charge-carrier recombination and thus enhanced the solar cell PCE.

2. Enhanced Efficiency of Sn–Pb Perovskite Cell by Ba Incorporation

In this study, we used a methylammonium (MA)-free composition of $Cs_{0.2}FA_{0.8}Pb_{0.5}Sn_{0.5}I_3$, where formamidinium (FA) is for enhanced thermal stability.[32] With an initial motivation of reducing the hole density in Sn–Pb NBG perovskites, we chose divalent metal cations, including cadmium (Cd^{2+}), ytterbium(II) (Yb^{2+}), Ba^{2+}, and samarium(II) (Sm^{2+}), with a similar radius to that of Sn^{2+} in order to fill the tin vacancies and thus decrease the hole density in Sn–Pb NBG perovskites, though they are shown not to occupy B sites in our followed study. Metal iodide salts of CdI_2, YbI_2, BaI_2, and SmI_2 were mixed into the 2.0 M $Cs_{0.2}FA_{0.8}Pb_{0.5}Sn_{0.5}I_3$ precursor solutions as additives with tuned concentrations. As shown in **Figure 1**A, a small amount of all these metal iodide salts (0.03–0.1 mol% compared to lead) enhanced the PCE of Sn–Pb perovskite solar cells when their concentrations were optimized. The PCE enhancement mainly came from an increase in open-circuit voltage (V_{OC}) and short-circuit current density (J_{SC}) (Table S1, Supporting Information). All of these metal cations showed the same trend, that a small amount increased the solar cell PCE, while too high a concentration reduced the PCE, as shown by the statistical data in Figure S1, Supporting Information. Among them, 0.1 mol % BaI_2 in $Cs_{0.2}FA_{0.8}Pb_{0.5}Sn_{0.5}I_3$ yielded the largest increase in PCEs. Thus, we fabricated 40 devices using 0.1 mol% BaI_2 as an additive in the perovskite precursor and compared their PV performance with pristine Sn–Pb perovskites. As shown in Figure 1B, the BaI_2 additive resulted in an increase in V_{OC}, J_{SC}, and fill factor (FF) of the Sn–Pb perovskite solar cells and thus enhanced the PCE from 19.2% to 20.5% on average. The champion small area (8 mm^2) device has a V_{OC} of 0.86 V, a J_{SC} of 31.5 mA cm^{-2}, a FF of 78.1%, and a PCE of 21.2%, which is a large increase compared to the pristine device (19.6%) as shown in Figure 1C.

The NBG perovskite devices with the BaI_2 additive exhibited an obvious increase of the external quantum efficiency (EQE) by ≈10% in the red-light region (600–1000 nm) (Figure 1D), which indicates a longer carrier diffusion length. Another indication of the enhanced carrier diffusion length in the NBG perovskite with BaI_2 is that the J_{SC} of the device stayed nearly unchanged when the thickness of the NBG perovskite layer was increased to 1.3 μm, while the control devices without BaI_2 rapidly lost its J_{SC} and FF when the MHP layer thickness was >1 μm (Figure 1E and Figure S2, Supporting Information). The Sn–Pb NBG perovskite devices with BaI_2 also exhibited larger V_{OC} and FF, especially when the perovskite films were thicker than 850 nm (Figure 1E), confirming that BaI_2 plays the role of suppressing non-radiative carrier recombination. To verify the thickness-dependent J_{SC} of the NBG perovskite solar cells with and without BaI_2, we measured their EQE spectra which were shown in Figure S3A,B, Supporting Information. The calculated J_{SC} based on the solar spectrum and EQE spectra of the solar cells with varied film thicknesses are summarized in Figure S3C, Supporting Information, which are very close to the results in Figure 1E.

We fabricated monolithic MHP–MHP tandem solar cells of the optimized Sn–Pb perovskites and a WBG (1.75 eV) perovskite of $Cs_{0.4}FA_{0.6}PbI_2Br$ with the device structure shown in Figure S4A,B, Supporting Information, shows the cross-sectional scanning electron microscope (SEM) image of a tandem cell. As shown in Figure S5, Supporting Information, and **Table 1**, the champion WBG single-junction solar cell had a V_{OC} of 1.23 V, a J_{SC} of 17.5 mA cm^{-2}, a FF of 80.3%, and a PCE of 17.3%. Figure 1F shows performance across 15 tandem devices which display an average PCE of 25.0 ± 0.48% with good reproducibility. As indicated in Figure 1G, the champion device had a high efficiency of 25.6% with a V_{OC} of 2.03 V, a J_{SC} of 15.8 mA cm^{-2}, and a FF of 79.4% under reverse J–V scan conditions, with a stabilized efficiency of 25.3% at a fixed operation bias of 1.70 V. The EQE spectra for the two subcells of the champion tandem solar cell are shown in Figure 1H, which gives the calculated J_{SC} of 15.7 mA cm^{-2} for both the WBG and the NBG subcells. This is well-balanced and close to the measured J_{SC}. As shown in Figure 1I, the cell with a larger area of 0.94 cm^2 had a high PCE of 24.2%, again agreeing with the measured stabilized efficiency of 24.1%. The efficiencies reported in this work for both small and large area all-perovskite tandem solar cells are comparable with the reported record efficiencies.[16,33] Figure S6, Supporting Information, shows the PV parameters of the encapsulated tandem solar cell under continuous 1-sun illumination in air ambient. It retained 95% of the initial PCE after being illuminated near the maximum power point condition for 350 h under continuous illumination and operation in line with ISOS-L-1 protocol.[34]

3. Optoelectronic Properties NBG Perovskites with Ba^{2+}

Figure 2A,B shows how 0.1 mol% BaI_2 additive impacts the optoelectronic properties of $Cs_{0.2}FA_{0.8}Pb_{0.5}Sn_{0.5}I_3$ where the

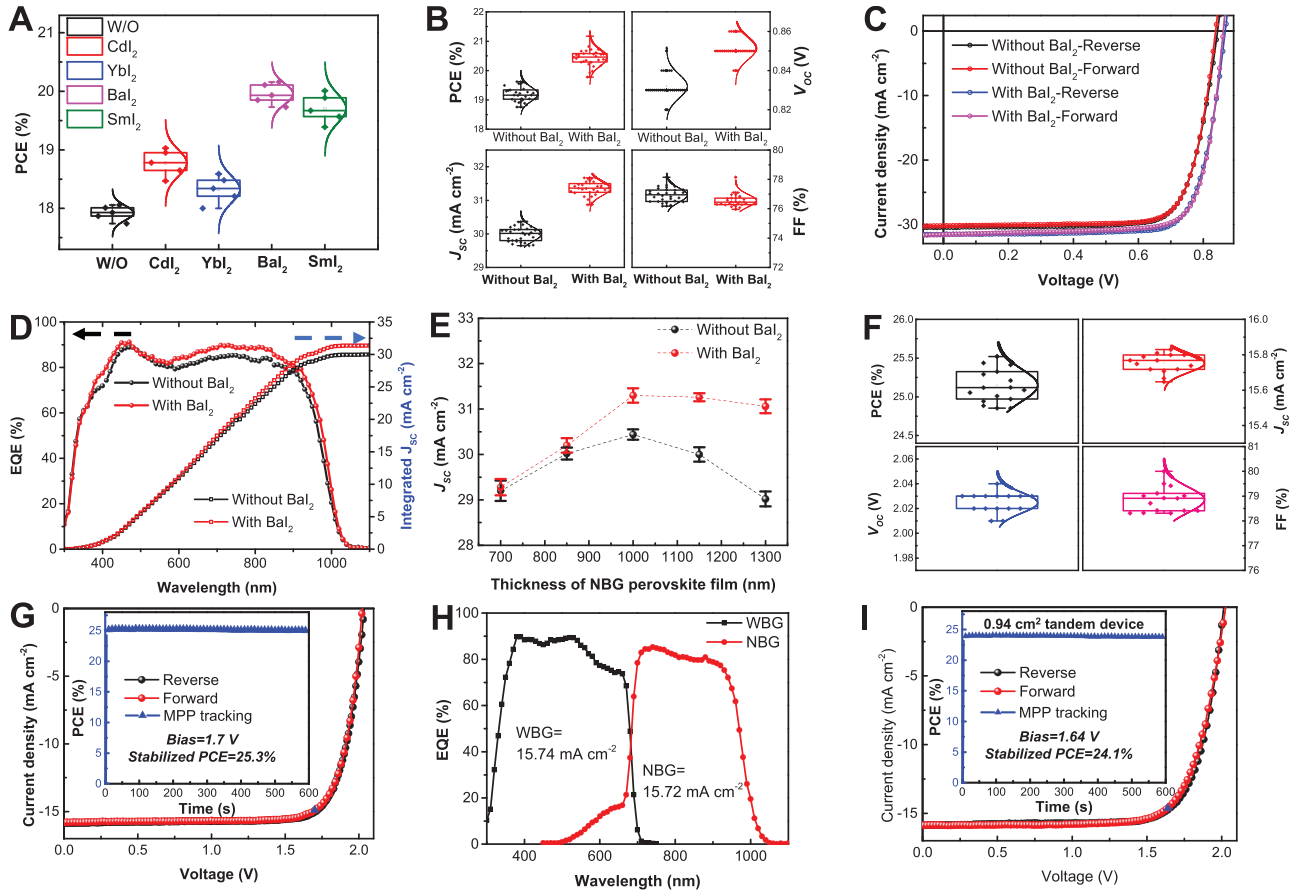

Figure 1. Sn–Pb perovskite with BaI_2 for efficient single-junction and tandem solar cells. A) Statistics of PCEs for single-junction devices with pristine Sn–Pb perovskite and perovskites with 0.03 mol% CdI_2, 0.1 mol% YbI_2, 0.1 mol% BaI_2, and 0.1 mol% SmI_2 which are optimized concentration for the highest efficiencies. For perovskites with each kind of additives, five devices were fabricated for statistics. B) PV parameter statistic of 30 devices of each type. C) Current density–voltage (*J–V*) curves under reverse and forward scanning, and D) EQE spectra for the champion single-junction devices with and without 0.1 mol% BaI_2. E) Thickness-dependent J_{SC} for single-junction solar cells based on Sn–Pb perovskites without and with 0.1 mol% BaI_2. For perovskites with each thickness, five devices were fabricated for statistics. F) PV statistics for 15 optimized tandem solar cells. G) *J–V* curves for the champion tandem device under reverse and forward scanning, inset is the steady-state PCE output at the bias of 1.70 V of the champion tandem device. H) EQE for the WBG and NBG subcells of the champion tandem solar cell. I) *J–V* curves for the champion 0.94 cm^2 tandem solar cell under reverse and forward scanning. The inset shows the stabilized PCE output at a bias of 1.65 V of the same device.

carrier recombination lifetime τ were measured by transient photovoltage (TPV) decay in operational devices and transient absorption (TA) on thin films. Both measurements resulted in an increase in carrier recombination lifetime from ≈1.3 to ≈1.9 μs with a 0.1% BaI_2 addition. This is the longest carrier recombination lifetime reported for Sn–Pb perovskites, and is comparable to the state-of-the-art pure Pb-based polycrystalline perovskite thin films, indicating a successful suppression of non-radiative charge recombination.[20,27] We further investigated these films using a unique combination of transient THz and transient reflection spectroscopy, from which individual carrier mobility (μ) and surface recombination velocities (SRV) could be extracted.[27,35–37] Figure 2C,D illustrates the transient THz spectra at 10 ps delay for Sn–Pb perovskite films with and without 0.1 mol% BaI_2, from which the sum of DC mobility (μ_{dc}) was extracted by using a Drude–Smith model (See Experimental Section for modeling details). The best-fit gives a sum of electron hole mobility ($\mu_{dc} = \mu_e + ¼_h$) of 36.50 ± 2.81 and 37.40 ± 2.88 $cm^2\ V^{-1}\ s^{-1}$ for Sn–Pb perovskite films without and with BaI_2, respectively. Figure 2E,F illustrates the surface carrier kinetics measured with transient reflection. By simultaneously modeling the decay of charge carriers with a global fitting procedure that includes both ambipolar diffusion ($\mu_{ab} = (\mu_e\mu_h)/(\mu_e + \mu_h)$) and surface recombination, best-fit values of μ_{ab} and SRV values were obtained. Introducing 0.1 mol% BaI_2 improved μ_{ab} values from 0.83 ± 0.06 to 0.95 ± 0.07 $cm^2\ V^{-1}\ s^{-1}$ and reaches a SRV values of 23 cm s^{-1}. With measured μ_{dc} and μ_{ab}, individual electron and hole mobility can be calculated. However, this method does not distinguish the mobility of an electron from that of hole, instead, it permits identification of the limiting carrier mobility. Our results indicate that the limiting carrier mobility of Sn–Pb perovskites increased from 0.85 to 0.98 $cm^2\ V^{-1}\ s^{-1}$ by introducing 0.1 mol% BaI_2, which corresponds to an increase in limiting carrier diffusion length from 1.70 to 2.13 µm (Table S2, Supporting Information). Such a long carrier diffusion length can enable the use of a thicker Sn–Pb perovskite thin film to harvest more photons (especially in the near-infrared region as shown in Figure 1D) and

Table 1. Photovoltaic parameters for single-junction and monolithic perovskite–perovskite tandem solar cells. Narrow bandgap (NBG) refers to the perovskite with a bandgap of 1.21 eV and wide bandgap (WBG) refers to the perovskite with a bandgap of 1.75 eV. All the solar cells reported in this work are measured with 5.9 mm^2 photomask unless differently specified.

Device configuration	Scan direction	PCE [%]	V_{OC} [V]	J_{SC} [mA cm^{-2}]	FF [%]
ITO/PEDOT:PSS/NBG/C_{60}/BCP/Cu	Reverse	19.6	0.84	30.2	77.3
ITO/PEDOT:PSS/NBG/C_{60}/BCP/Cu	Forward	19.5	0.83	30.2	77.8
ITO/PEDOT:PSS/NBG+BaI_2/C_{60}/BCP/Cu	Reverse	21.2	0.86	31.5	78.1
ITO/PEDOT:PSS/NBG+BaI_2/C_{60}/BCP/Cu	Forward	21.1	0.86	31.5	77.9
ITO/PTAA/WBG/C_{60}/SnO_2/Cu	Reverse	17.3	1.23	17.5	80.3
ITO/PTAA/WBG/C_{60}/SnO_2/GO/PEDOT:PSS/NBG+BaI_2/C_{60}/BCP/Cu (Champion cell)	Reverse	25.6	2.03	15.8	79.4
	Forward	25.3	2.02	15.8	79.3
ITO/PTAA/WBG/C_{60}/SnO_2/GO/PEDOT:PSS/NBG+BaI_2/C_{60}/BCP/Cu (Champion cell, 0.94 cm^2)	Reverse	24.2	2.01	15.8	76.2
	Forward	24.0	2.02	15.8	75.2

associated photocarriers. It is also noteworthy that the SRV of 23 cm s^{-1} for the 0.1 mol% BaI_2-incorporated Sn–Pb perovskite is among the lowest reported for Sn–Pb perovskites.[27]

The addition of 0.1 mol% BaI_2 did not cause any notable change to the morphology of perovskites from the scanning electron microscopy (SEM) images of Sn–Pb perovskite films (Figure S7, Supporting Information), nor changed the crystallinity of the film from the X-ray diffraction (XRD) study (Figure S8, Supporting Information), nor did it cause any notable change of the absorption spectrum (Figure S9, Supporting Information). Light intensity-dependent V_{OC} measurement was carried out to assess the diode ideality factors. As shown in Figure S10, Supporting Information, the pristine Sn–Pb perovskite solar cell had an ideality factor of 1.53 which is comparable to previously reported results.[17] After introducing BaI_2 in the Sn–Pb perovskite, the ideality factor further decreased to 1.32, consistent with the BaI_2 suppressing carrier recombination in the devices. The NBG perovskite solar cells with BaI_2 also showed relatively low dark current in both forward and reverse bias conditions, as indicated in Figure S11, Supporting Information, demonstrating that the incorporation of BaI_2 results in a lower residual carrier density in the Sn–Pb perovskite.

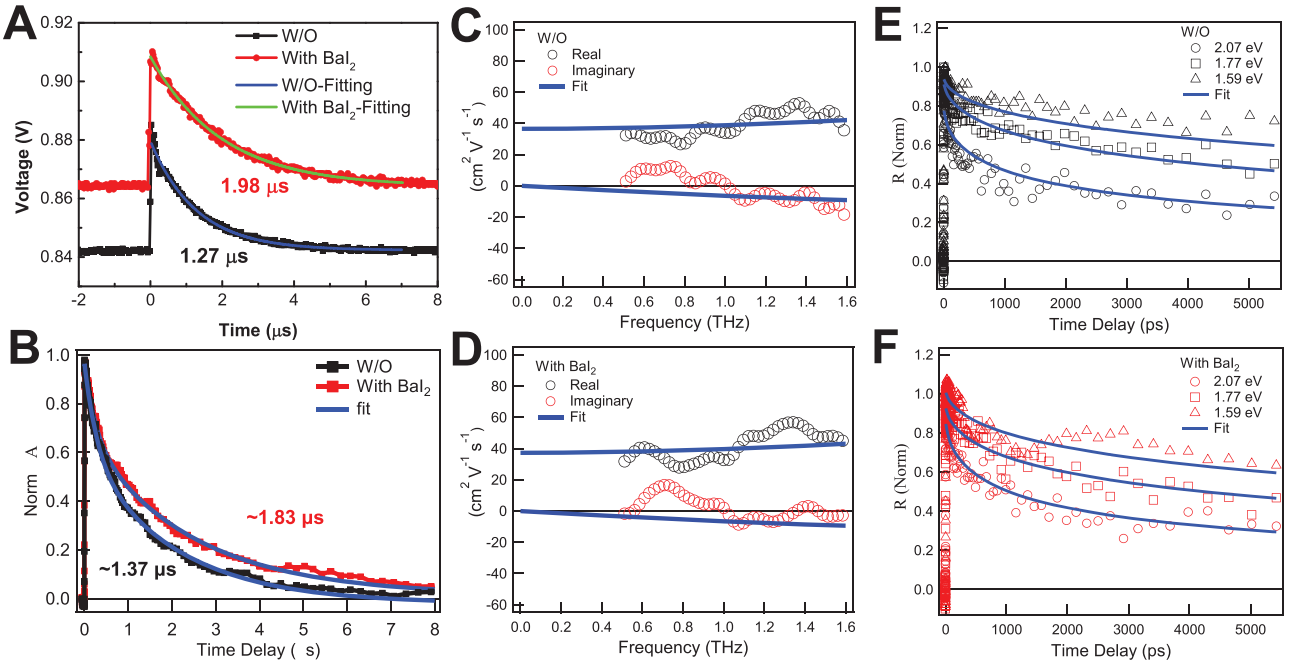

Figure 2. Influence of Ba^{2+} on optoelectronic and transport properties. A) Transient photovoltage decay (TPV) with single exponential fit and B) transient absorption (TA) kinetics with biexponential fits (blue solid line) of Sn–Pb NBG perovskites films with and without 0.1% BaI_2. With BaI_2 incorporation, the measured average carrier lifetime $\langle\tau\rangle = \frac{A_1\tau_1 + A_2\tau_2}{A_1 + A_2}$ increases from ≈1.3 to ≈1.9 µs. C,D) Comparison of transient THz spectra at 10 ps delay of low-bandgap perovskites without (C) and with (D) BaI_2. The spectra are modeled with Drude–Smith model (see Supporting Information) to extract the sum of electron and hole mobility. E,F) Comparison of surface carrier dynamics with fit (blue solid line) measured with transient reflectance spectroscopy of low-bandgap perovskite thin films prepared without (E) and with (F) the use of 0.1% BaI_2. From the measurement, ambipolar diffusion constant and surface recombination velocity can be extracted.

4. Gradient Doping in Sn–Pb Perovskite Films by Ba^{2+} Ions

The optimal BaI_2 concentration of 0.1 mol% is too small to induce an obvious lattice constant change to be observed by a standard XRD measurement. To find out whether Ba^{2+} can get into the lattice, we intentionally added 2, 5, and 10 mol% of BaI_2 into $Cs_{0.2}FA_{0.8}Pb_{0.5}Sn_{0.5}I_3$. As shown in **Figure 3**A,B, the large amount of BaI_2 shifted the XRD peaks to smaller diffraction angles and resulted in an increase in the lattice constant along all directions. The lattice expansion suggests that Ba^{2+} cations can be incorporated into the lattice of Sn–Pb perovskites by locating at the A site, B site, and interstitial site. Density functional theory calculations using Heyd–Scuseria–Ernzerhof (HSE) hybrid functional with the consideration of spin–orbital coupling (SOC) for Pb 6 p orbital reveal that while the Sn vacancy is a shallow acceptor, Ba^{2+} cations located at the A site (Ba_{Cs}) and the interstitial site (Ba_{int}) in $CsSn_{0.5}Pb_{0.5}I_3$ are shallow donors, as illustrated in Figure 3C. Since the conduction band minimum (CBM) of $CsSn_{0.5}Pb_{0.5}I_3$ is derived from Pb 6 p and I 5p states (Figure S12, Supporting Information), the strong SOC of Pb 6 p orbital lowers the energy position of the CBM. As a result, the relatively high energy lying Ba 6s state makes Ba_{Cs} and Ba_{int} rather shallow donors in $CsSn_{0.5}Pb_{0.5}I_3$. At the same time, Ba^{2+} cations at B sites are isovalent dopants and do not change the carrier density. The calculated formation energies under the I-rich conditions with an assumption of Fermi level at the middle of the bandgap of mixed Sn–Pb perovskite are 0.145, 0.695, and 4.27 eV for 1+-charged Ba_{Cs}, 2+-charged Ba_{int} and charge neutral Ba_{Sn} (Ba on Sn site), suggesting that most Ba cations doped in mixed Sn–Pb perovskite are likely at Cs sites or interstitial sites, acting as shallow donors. Considering the expanded lattice of perovskite after introducing Ba ions, Ba ions should occupy the interstitial sites. Therefore, Ba incorporation into interstitial sites compensates the p-doping introduced by Sn vacancies. The regions with sufficient Ba cations could be turned into n-type as similar inversion could be expected with Sr^{2+} doping,[38] depending on the concentration of Ba^{2+} cations.

To evaluate if the Ba^{2+} cations suppress p-doping in Sn–Pb perovskites, we conducted drive-level capacitance profiling (DLCP) measurements to ascertain the doping concentration in the perovskite layer. DLCP has been recently demonstrated by our group to measure the charge trap distribution in MHP solar cells,[29] and can also profile free carrier distribution by using a high ac frequency that trapping–detrapping charges cannot respond to quickly enough. **Figure 4**A shows the spatial distribution of shallow traps and free carriers at the relatively high ac frequency of 500 kHz. Here the profile distance represents the distance from perovskite/C_{60} interface. The pristine Sn–Pb perovskite without Ba^{2+} had a minimum doping density of $\approx 1.0 \times 10^{15}$ cm^{-3} which is comparable to the reported value

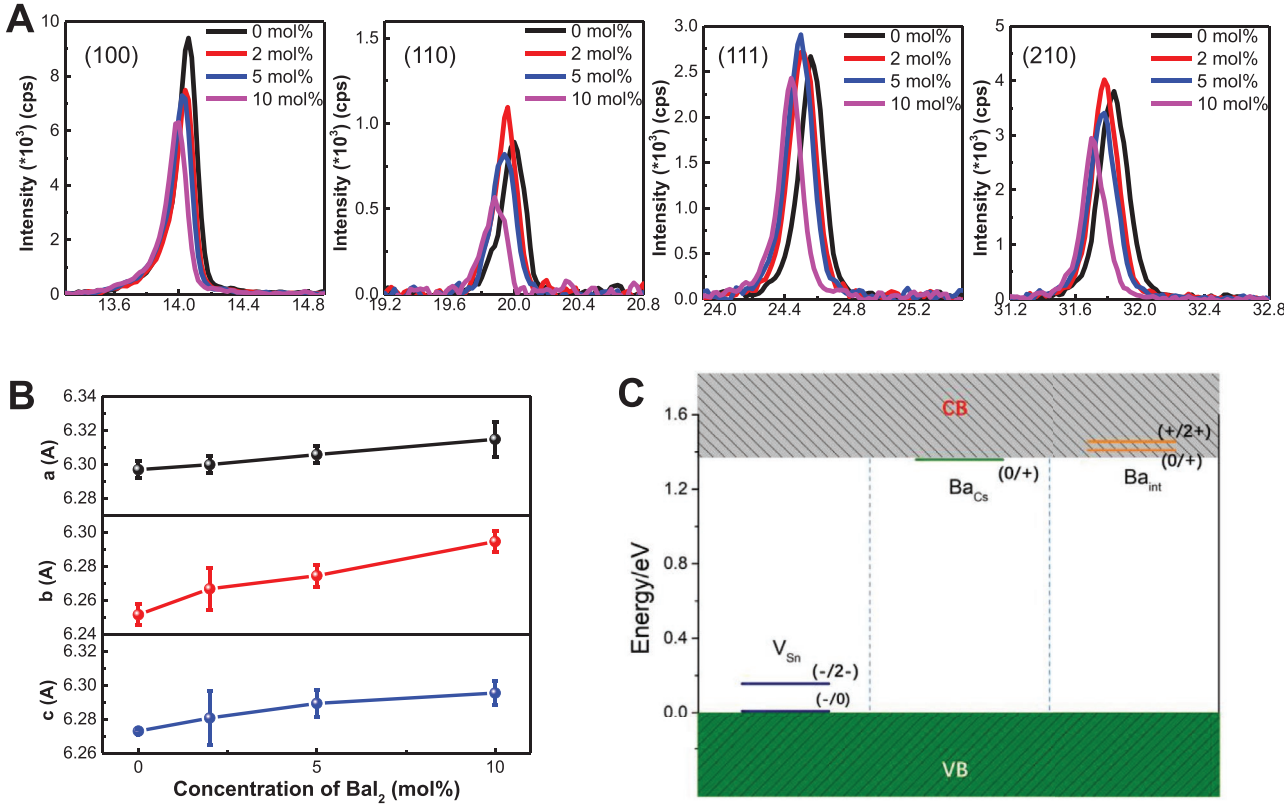

Figure 3. XRD characterization for Sn–Pb perovskites with BaI_2. A) XRD patterns for Sn–Pb perovskites with 0, 2, 5, and 10 mol% BaI_2 added in precursor solutions. B) Lattice constants for Sn–Pb perovskites with 0, 2, 5, and 10 mol% BaI_2 calculated from the XRD pattern. Five samples of NBG perovskite films with each concentration of BaI_2 were measured for lattice constants statistic. C) HSE spin–orbital coupling (SOC) calculated transition energy levels of V_{Sn}, Ba_{Cs}, and Ba_{int}.

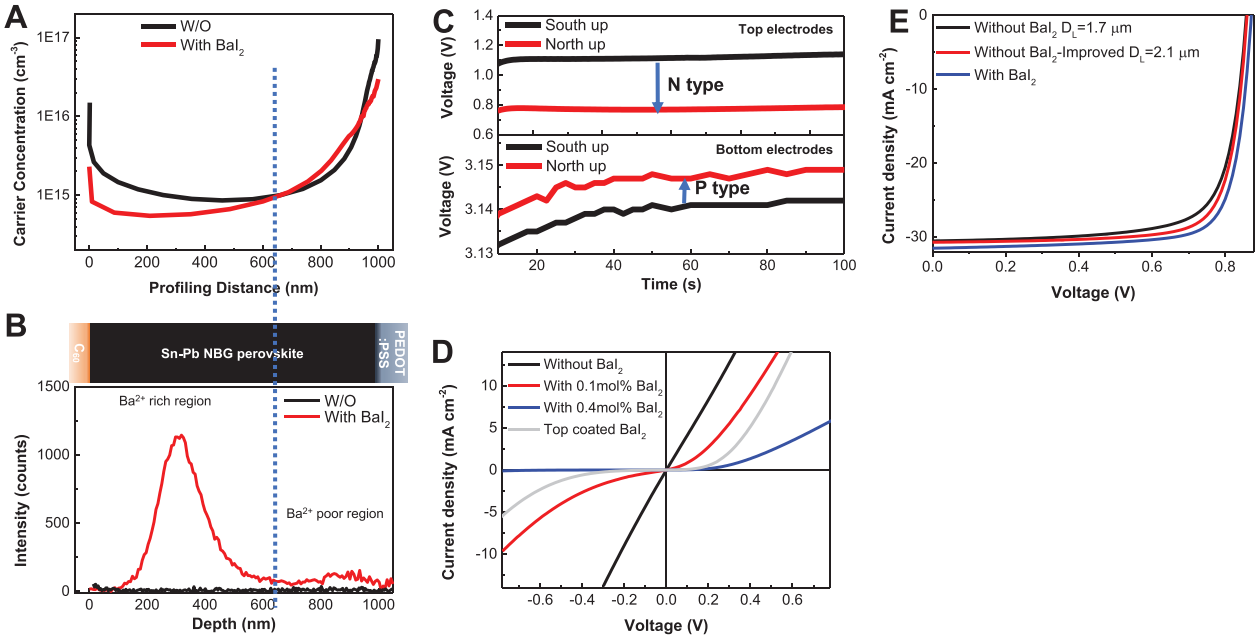

Figure 4. BaI_2-induced gradient doping in Sn–Pb perovskite. A) DLCP and B) TOF-SIMS measurements for Sn–Pb perovskites without and with 0.1 mol% BaI_2. The majority of the Ba^{2+} resides in the top 600 nm of the film. C) Time-dependent Hall voltages for Sn–Pb perovskite with 0.1 mol% BaI_2 with Au electrodes deposited on the bottom and top surfaces of the perovskite film. Increased or decreased Hall voltages upon flipping the magnetic field direction indicate that top and bottom surfaces of the Sn–Pb perovskites with 0.1 mol% BaI_2 were n-type and p-type, respectively. D) *J–V* curves scanned under dark for symmetrical devices of Au (50 nm)/perovskite (1 μm)/Au (50 nm)/glass. The perovskite layers were pristine Sn–Pb perovskite, perovskite introducing 0.1 mol% and 0.4 mol% BaI_2, and perovskite top coated by BaI_2 (0.4 mg ml^{-1} in IPA), respectively. E) SCAPS simulated *J–V* curves for solar cells based on uniform p-type perovskite layer (without BaI_2), the same p-type layer (without BaI_2) with an improved carrier diffusion length from 1.7 to 2.1 μm by enhancing electron mobility from 0.85 to 1.5 $cm^2\ V^{-1}\ s^{-1}$, and p–n double perovskite layers (with BaI_2) with a p–n homojunction.

for reduced Sn^{2+} vacancies by metallic Sn in Sn–Pb perovskites.[20] After introducing 0.1 mol% BaI_2, the doping density decreased in the top 600 nm portion of the perovskite film, and reached a minimum doping level of 5.0×10^{14} cm^{-3} which is the lowest among all reported Sn–Pb perovskite multicrystal films. However, in a notable and striking contrast, the carrier density did not show as large a change in the bottom 400 nm of the perovskite film. To clarify the nonuniform doping induced by Ba^{2+} cations, we measured their distribution through the Sn–Pb perovskite film thickness using time-of-flight secondary ion mass spectrometry (TOF-SIMS). Figure 4B shows the spatial distribution of Ba^{2+} cations in the Sn–Pb perovskite films with and without 0.1 mol% BaI_2. Most Ba^{2+} cations were found to reside in the top 600 nm region, which is in excellent agreement with the heterogeneous doping profile induced by Ba^{2+} cations. This study not only confirms that the Ba^{2+} cations indeed decrease hole density for the top portion of Sn–Pb perovskite films, but also indicates the presence of a homojunction or band bending in the Sn–Pb perovskites due to the heterogeneous doping mirroring the Ba^{2+} profile.

We conducted Hall effect measurements to verify the different doping levels at the top and bottom regions of the Sn–Pb perovskite films by depositing Hall electrodes on the top and bottom surface of the Sn–Pb perovskite films with a geometry shown in Figure S13A, Supporting Information. By measuring the direction and magnitude of Hall voltage change after switching the magnetic field direction, the doping type and concentration of the films can be qualitatively determined. The film without BaI_2 additive showed p-type behavior for measurements conducted at both the top and bottom surfaces (Figure S13B, Supporting Information). In contrast, the film with 0.1 mol% BaI_2 exhibited n-type behavior for the top portion of the films while the bottom portion was still p-type (Figure 4C). This result not only confirms the heterogeneous carrier distribution and carrier density decrease induced by Ba^{2+} cations, but also shows that the top part of perovskite film was converted to n-type.

To further verify the gradient doping, we fabricated devices with symmetrical electrodes of Au/perovskite/Au using pristine and Ba^{2+}-incorporated Sn–Pb perovskites, respectively. As shown in Figure 4D, the device based on pristine perovskite has a linear dark current, suggesting similar electronic properties at top and bottom surfaces. However, the dark current of the device with 0.1 mol% BaI_2 showed a clear rectification behavior, and the rectification ratio increased when the concentration of BaI_2 in Sn–Pb perovskite increased to 0.4 mol% (Figure 4D). Spin-coating BaI_2 solution on the top of the pristine Sn–Pb perovskite resulted in a device with rectification behavior comparable to that those with 0.4 mol% BaI_2 (Figure 4D). All these results support the notion that incorporation of Ba^{2+} can n-dope Sn–Pb perovskite. Naturally, the gradient doping across the perovskite film suggest the formation of a p–n homojunction with n-side near C_{60} and p-side near poly(3,4-ethylenedioxythiophene):poly(styrene-sulfonate) (PEDOT:PSS) ($n^+(C_{60})$/n(top film)/p(bottom film)/(p^+)PEDOT:PSS), and thus the built-in electric field direction favors charge separation. Compared with

pristine perovskites whose configuration is ($n^+(C_{60})$/p(film)/(p^+)PEDOT:PSS), the existence of the homojunction could contribute to the lengthened radiative carrier recombination lifetime and carrier diffusion length, as we observed in those measurements. It is noted that the built-in field may contribute a drift component to the increased diffusion length by increasing the charge recombination lifetime. To figure out what dominates the observed device efficiency enhancement, we simulated the *J–V* curves and the energy diagrams for the solar cells based on pristine (uniformly p-doped) and gradient doping Sn–Pb perovskites with doping profile shown in Figure S14, Supporting Information. We also simulated a case that the uniform p-doped Sn–Pb perovskites have a same diffusion length with that with a p–n homojunction by increasing the mobility of charges to find out the role of p–n junction. As shown in Figure 4E, simply increasing the carrier diffusion length does not notably increase J_{SC}, though it slightly enhanced device FF. The gradient doping across the perovskite could lead to an enhanced J_{SC} from 30.6 to 31.4 mA cm^{-2}, which is consistent with our experimental result. This result highlights the importance of the p–n homojunction in boosting the efficiency of Sn–Pb perovskite solar cells by reducing the bulk charge recombination.

To understand how the gradient Ba^{2+} distribution was formed, we investigated the in situ film formation process using grazing-incidence X-ray diffraction (GIXRD). To generate some depth resolution, the X-ray incident angle was varied to be 1° or 4° so that the X-ray signal came from either only the top 150 nm portion (C_{60} side) of the films, or the whole films, respectively. We changed the film annealing time and measured the composition of the films using GIXRD. As shown in **Figure 5**A, the film right after spin-coating without annealing already had perovskite phase formed in the top surface of the film (C_{60} side). However, it showed an obvious diffraction peak of lead(II) iodide (PbI_2)-dimethyl sulfoxide (DMSO) intermediate phase from the bottom portion of the film. After annealing for 1 s, the PbI_2-DMSO peak disappeared and a very weak PbI_2 peak emerged, suggesting the rapid evaporation of DMSO and the formation of a small amount of PbI_2 at the bottom of the perovskite film (PEDOT side). After annealing for 2 s, most of the PbI_2 peak disappeared, indicating the crystallization process was basically completed. The GIXRD results suggest that the perovskite grew from the top to bottom accompanied with the evaporation of DMSO, which is consistent with our recent study.[39] Then, TOF-SIMS was used to study the ion distribution in the perovskite films during their growth process. As shown in Figure S15, Supporting Information, Cs^+ and FA^+ cations were uniformly distributed across the film during the whole growth process while the Pb, Sn, and Ba ions showed interesting changes during the solid film formation process. The trend for the variation of Pb distribution during the annealing process was very similar to that of Sn, as illustrated in Figure S16, Supporting Information. Before annealing, Pb and Sn concentrated at the top 200 nm and bottom 600 nm portion of the film, because the perovskite phase formed on the top and the PbI_2/tin(II) iodide (SnI_2)-DMSO intermediate phase remained at the bottom of the undried film. After annealing, their distribution gradually became uniform. The distribution of Ba cations in the unannealed film was like that of Pb or Sn, while annealing drove most of the Ba cations to move up from the bottom region of the film, as shown in Figure 5B. We noticed that the upward movement of the Ba cations was

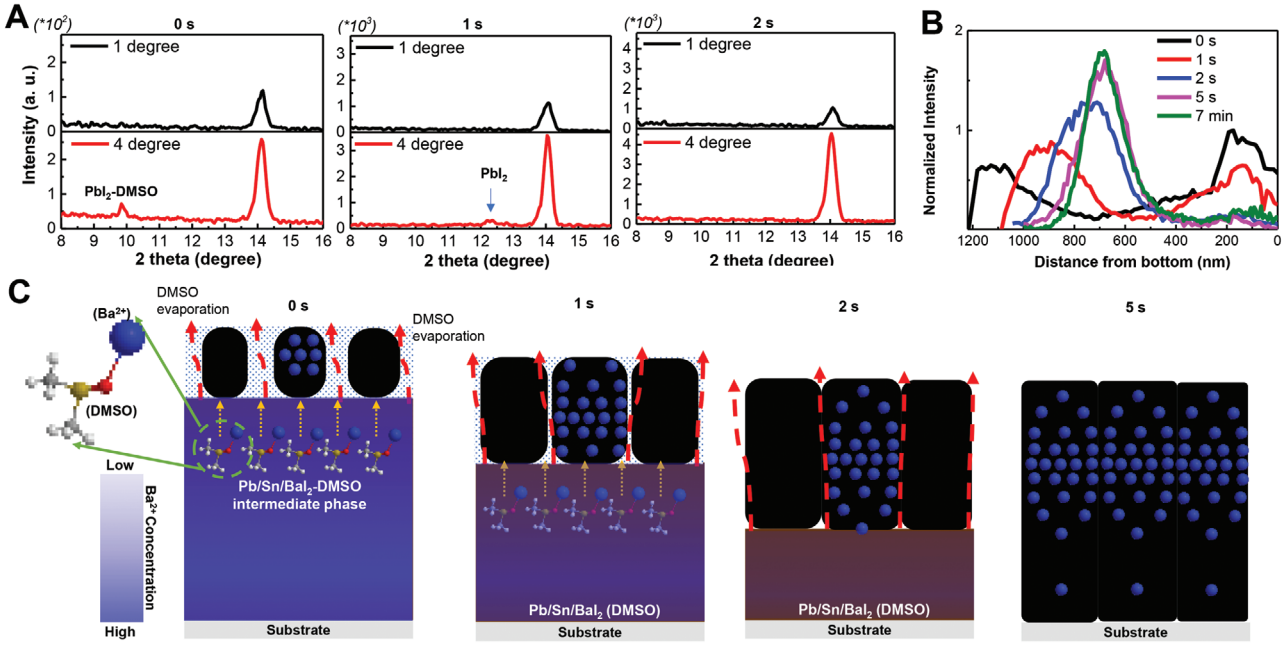

Figure 5. Mechanism for the gradient Ba ion distribution in Sn–Pb perovskite films. A) GIXRD patterns for 0.1 mol% BaI_2-incorporated Sn–Pb perovskite films under grazing angles of 1° and 4°, respectively. The perovskite films were annealed for 0, 1, and 2 s, respectively. B) Normalized depth-profile of Ba^{2+} ion in perovskite films with varied annealing duration from 0 s to 7 min. C) Schematic diagram for film growth process of Ba-incorporated Sn–Pb perovskite, in which the black squares represent the perovskite grains, the blue dots represent the Ba^{2+} in grains, and the gradient blue color represents the concentration of Ba^{2+}.

commensurate with DMSO evaporation, and thus we speculate that Ba cations were brought up by DMSO molecules during the evaporation process. Fourier transform infrared (FTIR) spectroscopy results shown in Figure S17, Supporting Information, illustrate that Ba cations have stronger interaction with DMSO than Pb cations, supporting our proposed mechanism. As the amount of Ba is much lower than Pb and Sn, the Ba^{2+} can only participate in the nucleation and early growth process as illustrated in Figure 5C, making Ba^{2+} mainly distributed in the top 600 nm of the film. This unique nonuniform distribution of Ba^{2+} cations results in the gradient doping in the Sn–Pb perovskite, which generates a homojunction.

Previous studies reported that the formation of the p–n homojunction can enhance the PCE of MHP solar cells[40–43] while the junction formed by unintentional doping from iodide defects might not be stable due to their facile migration.[44–46] The p–n junction formed by nonuniform Ba cation distribution should be much more stable due to the much larger energy barrier for cation migration. To evaluate how stabile the homojunction is, we annealed the films at 85 °C for 300 h, and then checked the Ba^{2+} distribution again. As shown in Figure S18, Supporting Information, on the top 600 nm of the perovskite film after heating, the Ba^{2+} rich region still keeps a similar distribution.

5. Conclusions

We have demonstrated the gradient doping of Sn–Pb NBG perovskites via incorporation of barium cations. The incorporation of 0.1 mol% of BaI_2 heterogeneously n-doping in Sn–Pb perovskites is due to the uniform distribution of Ba^{2+} cations from the top-to-the-bottom of the perovskite films. The result is a p–n homojunction with the built-in electric field direction favoring charge separation, which enhances the carrier recombination lifetime and leads to a photocurrent enhancement. The p–n homojunction caused by the gradient doping of Sn–Pb perovskite by Ba interstitials boosted the PCE of Sn–Pb perovskite solar cells from ≈19% to over 21%. The BaI_2-incorporated Sn–Pb perovskites boosts the device efficiency of small-area (5.9 mm^2) and large-area perovskite–perovskite tandem solar cells (0.94 cm^2) to 25.3% and 24.1%, respectively. The findings introduce an effective strategy to selectively decrease the hole density in the Sn–Pb perovskite and changing its doping type, enabling a method of spontaneously forming an advantageous homojunction inside perovskite films without needing a complex multilayer coating process.

6. Experimental Section

Materials: Formamidinium iodide (FAI) was purchased from Greatcell Solar company. PbI_2 (99.999%), lead(II) bromide ($PbBr_2$, 99.999%), SnI_2 (99.999%), tin(II) fluoride (SnF_2), cesium iodide (CsI, 99.999%), BaI_2 (anhydrous, 99.995%), CdI_2, YbI_2, SmI_2, phenethylammonium bromide (PEABr), phenylethylamine hydrochloride (PEACl), acetone, isopropanol alcohol (IPA), toluene, anhydrous DMSO, poly(bis(4-phenyl)(2,4,6-trimethylphenyl)amine) (PTAA), bathocuproine (BCP), anhydrous ethyl acetate, choline chloride, and anhydrous *N*,*N*-dimethylformamide (DMF) were purchased from Sigma-Aldrich. C_{60} was purchased from NANO-C company. PEDOT:PSS (Clevios P VP AI 4083) was purchased from Heraeus company. Aqueous graphene oxide (GO) solution was purchased from Graphene Supermarket. $MAPbCl_3$ single crystals were synthesized in our lab by a previously reported method.[47]

Perovskite Precursor Solutions Preparation: For the pristine Sn–Pb NBG perovskite (1.21 eV), 2.0 M $Cs_{0.2}FA_{0.8}Pb_{0.5}Sn_{0.5}I_3$ precursor solution was prepared by dissolving 1.60 M FAI, 0.40 M CsI, 1.00 M PbI_2, 1.00 M SnI_2, 0.10 M SnF_2, and 2.5 mg mL^{-1} PEACl in a mixed solvent (volume ratio of 1:3) of DMSO and DMF and stirred at room temperature overnight. For the NBG perovskite solution used for the additive study on varied metal iodine salts with varied concentrations, equal stoichiometric PbI_2/SnI_2 (1:1) was reduced from the recipe of pristine precursor solution.

For the WBG perovskite (1.75 eV), 1.35 M $Cs_{0.4}FA_{0.6}PbI_2Br$ precursor solution was prepared by dissolving 0.54 M CsI, 0.81 M FAI, 0.68 M $PbBr_2$, 0.67 M PbI_2, 4 mol% $MAPbCl_3$ single crystals, and 1.0 mg mL^{-1} PEABr in mixed solvent of DMSO and DMF (volume ratio of 3:7) and stirred at room temperature for overnight. All the precursor solution was filtered with 0.22 µm poly(tetrafluoroethylene) filters before use.

Fabrication of Single-Junction NBG Perovskite Solar Cells: PEDOT:PSS was spin-coated onto the ITO substrates at 5000 rpm. for 20 s, followed by annealing at 105 °C for 30 min. Then, the pristine Sn–Pb NBG perovskite precursor with 0.03 mol% CdI_2,[17] 0.05–0.4 mol% YbI_2, 0.05–0.4 BaI_2, and 0.05–0.4 mol% SmI_2 was spin-coated onto PEDOT:PSS. The perovskite film thick was controlled by varying the spin-coating processes and measured with profilometry. They were 6000 rpm for 50 s for 700 nm, 4000 rpm for 50 s for 850 nm, 1500 rpm for 4 s followed by 4000 rpm for 40s for 1000 nm, 1500 rpm for 10s followed by 4000 rpm for 40 s for 1150 nm, and 1500 rpm for 15 s followed by 3000 rpm for 40 s for 1300 nm. Then 150 µL ethyl acetate was quickly casted on the top of perovskite 5 s before the end of the spin-coating process. Then it was annealed at 130 °C for 7 min before depositing ETLs. Finally, 25 nm C_{60}, 8 nm BCP, and 80 nm copper electrode were sequentially thermal evaporated onto these perovskite films.

Fabrication of Single-Junction WBG Perovskite Solar Cells: 2 mg mL^{-1} PTAA dissolved in toluene was spin-coated onto ITO substrates at 4500 rpm for 20 s, followed by annealing at 100 °C for 10 min. Then, WBG perovskite precursor solution was spin-coated onto PTAA layers at 4500 rpm for 40 s and begun to blow the films with N_2 at 20th second of the spin-coating process. Subsequently, the samples were annealed at 65 °C for 5 min and 100 °C for 10 min. Then 1 mg mL^{-1} PEABr in IPA solution was spin-coated on the as-prepared perovskites before annealing at 100 °C for 10 min. Subsequently 1 mg mL^{-1} choline chloride in IPA solution was spin-coated on perovskites followed with annealing at 100 °C for 30 min. Finally, 20 nm C_{60}, 8 nm BCP, and 80 nm copper electrode were sequentially thermal evaporated onto these perovskite films.

Fabrication of Perovskite–Perovskite Tandem Solar Cells: Fabrication of the WBG subcells was done using the same process as the abovementioned methods for WBG single-junction solar cells until the step of the C_{60} layer. 15 nm compact SnO_2 layer was deposited by ALD with 130 cycles at 85 °C. Then the samples were post-annealed in air ambient at 105 °C for 30 min. Aqueous GO solution was spin-coated on the top of SnO_2 followed by annealing at 105 °C for 1 h. PEDOT:PSS, Sn–Pb NBG perovskite films, C_{60}, BCP, and copper electrodes were deposited with the same process as the abovementioned methods for NBG single-junction solar cells

Electrical Measurements: Current density–voltage (*J*–*V*) measurement was performed under the simulated AM 1.5 G irradiation (100 mW cm^{-2}) produced by a xenon-lamp-based solar simulator (Oriel 94043A, 450 W AAA Solar Simulator). The light intensity was calibrated by a Reference Solar Cell and Meter (91150, Newport). A Keithley 2400 source meter was used for the *J*–*V* measurements. All *J*–*V* measurements were taken under 100 mW cm^{-2} illumination at reverse scan mode with a scan rate of 0.05 V s^{-1}. EQE measurements were conducted with a Newport QE measurement kit by focusing a monochromatic beam of a Bruker Vertex 80v Fourier Transform Interferometer with tungsten lamp source onto the devices. Then the photocurrent was obtained through Stanford Research SR570 current preamplifier. Samples were calibrated to a Newport calibrated reference silicon solar cell with a known EQE. For single-junction solar cells, no light bias was used for the EQE measurement. For tandem solar cells, light bias of blue light (≈470 nm)

and infrared light (≈940 nm) with light intensity of ≈0.3 sun were used to measure the EQE of the NBG and WBG subcells, respectively. The Hall effect measurement for devices with structure as shown in Figure S11A, Supporting Information, was taken as per tour previously reported method.[48] A constant current (I) of 1 or 3 µA was applied on the I^- and I^+ electrodes. And the Hall voltage (V_{Hall}) was measured between the V_H electrodes after applying a magnetic field to the samples. When a north-pole-face-down magnetic fields was applied, the measured voltage between the V_H electrodes electrodes was smaller than that measured when a south-pole-face-down magnetic fields was applied, indicating an n-type characteristic of the perovskite film. The V_{Hall} was the half of the total voltage change when the magnetic field direction was flipped. The maximum applied magnetic field intensity (B) was 0.3 T. The work area of all the solar cells reported in this work unless specified was 8 mm^2, which was defined by the overlap of ITO and Cu electrode. For an accurate measurement of device photocurrent, we applied a photomask with a smaller area of 5.9 mm^2 for all the 8 mm^2 small-area devices, as shown in each Figure captions. All the devices, including single-junction and all-perovskite tandem solar cells were encapsulated in N_2 fill glovebox using epoxy and cover glass. All the measurements for the encapsulated solar cells were taken in air.

Characterization: Transient photovoltage decay (TPV) measurement was taken by using a 337 nm laser pulse (SRS NL 100 Nitrogen Laser, frequency of 10 Hz and pulse width of <3.5 ns) and collecting signal by a digital oscilloscope (DOS-X 3104A) under 1-sun illumination. DLCP measurement was performed by using an Agilent E4980A precision LCR meter.[29] Nanosecond TA spectra were collected using an EOS system and a Coherent Libra Ti: sapphire laser, with an output of 800 nm at 1 kHz. The transient THz measurements were performed by a pump–probe spectrometer and the transient reflectance measurements were performed by a pump–probe spectrometer (Helios, ultrafast systems). An ION-TOF TOF-SIMS V spectrometer was utilized for depth profiling of the perovskite utilizing methods covered in detail in previous reports.[49] More details are shown in Supporting Information. The SEM images were taken from a Hitachi S-4700 Cold Cathode Field Emission SEM. Light intensity-dependent measurements for ideality factors were measured with a series of neutral optical density filters. Film thicknesses were measured by a Bruker Dektak XT stylus profiler. PL spectra were characterized by a Horiba iHR320 Imaging Spectrometer. XRD and GIXRD were carried out on a Rigaku SmartLab theta–theta diffractometer with an X-ray tube at 3.0 kW. This was configured with Cu Kα radiation (wavelength of 1.5418 Å). UV–vis–NIR absorbance was characterized by PerkinElmer Lambda 1050 UV–vis–NIR Spectrophotometers equipped with an integrating-sphere. FTIR spectroscopy was characterized by PerkinElmer FTIR spectrometer. The software SCAPS3308 was used to simulate the J–V curve and band diagram for NBG solar cells based on uniformly and heterogeneously doped Sn–Pb perovskites, respectively.

Computation Details: We used the Perdew–Burke–Enzerhof (PBE) functional for geometry optimization and HSE + SOC for calculations of electronic structure and defect energy levels.[50,51] The optimized mixing fraction of exact exchange was 0.37, which produced a bandgap of 1.37 eV for the $CsSn_{0.5}Pb_{0.5}I_3$ bulk. All calculations were performed with the Vienna Ab initio Simulation Program (VASP).[52] A $2 \times 2 \times 2$ host supercell with well-mixed Sn and Pb atoms was used for the calculations. The formation energy of defect D with charge q was calculated according to the formula:

$$\Delta E(D,q) = E(D,q) - E(\text{bulk}) \pm \mu(D) + qE_{\text{Fermi}} \quad (1)$$

where $E(D,q)$ is the total energy of the supercell containing the defect with charge q, E(bulk) is the total energy of the supercell without defect (bulk), $\mu(D)$ is the chemical potential of the defect atom that had been removed or added, and E_{Fermi} is the Fermi level, which was set to be the valence band maximum in this study. For compounds, $\mu(D)$ was constantly changing under different synthesis conditions. For comparison purpose, we only calculated defect formation energies under one synthesis condition, that is, I-rich. Therefore $\mu(I)$ was calculated from solid I.

Supporting Information

Supporting Information is available from the Wiley Online Library or from the author.

Acknowledgements

This material was based upon work supported by the U.S. Department of Energy's Office of Energy Efficiency and Renewable Energy (EERE) under Solar Energy Technologies Office (SETO) Agreement Numbers DE-EE0008749. The work at the National Renewable Energy Laboratory and University of Toledo was supported as part of theCenter for Hybrid Organic Inorganic Semiconductors for Energy (CHOISE), an Energy Frontier Research Center funded by the Office of Basic Energy Sciences, Office of Science within the U.S. Department of Energy. This work was authored in part by Alliance for Sustainable Energy, LLC, the manager, and operator of the National Renewable Energy Laboratory for the U.S. Department of Energy (DOE) under Contract No. DE-AC36-08GO28308. The views expressed in the article do not necessarily represent the views of the DOE or the U.S. Government. For the theoretical calculations, the authors used the high-performance computing system of the National Renewable Energy Laboratory (NREL).

Conflict of Interest

The authors declare no conflict of interest.

Author Contributions

Z.Y. and X.C. contributed equally to this work. J.H. and Z.Y. conceived the idea. J.H., Z.Y., and X.C. designed the experiments. Z.Y. fabricated all the devices and conducted the characterization. X.C. and M.C.B. investigated carrier properties through TA and THz measurements for the Sn–Pb perovskites. G.Y. deposited the ALD SnO_2 for tandem solar cells. Z.N. and S.X. studied the DLCP of Sn–Pb perovskite solar cells. Z.N. performed and analyzed the Hall effect measurement. X.C. and S.P.H. measured and analyzed the TOF-SIMS for the perovskites. B.C. measured the EQE spectra and took the SEM images. S.C. did the GIXRD measurements and analysis. C.Y. and Y.Y. did the computation. X.X. studied the XRD measurement. J.H., Z.Y., and X.C. wrote the paper, and all authors reviewed the paper. J.J.B. analyzed the data and revised the paper.

Data Availability Statement

The data that support the findings of this study are available from the corresponding author upon reasonable request.

Keywords

all-perovskite tandem solar cells, gradient n-doping by barium, homojunctions, Sn–Pb perovskite solar cells, ununiform distribution

Received: December 19, 2021
Revised: February 5, 2022
Published online: March 11, 2022

[1] A. Kojima, K. Teshima, Y. Shirai, T. Miyasaka, *J. Am. Chem. Soc.* **2009**, *131*, 6050.
[2] M. M. Lee, J. Teuscher, T. Miyasaka, T. N. Murakami, H. J. Snaith, *Science* **2012**, *338*, 643.

[3] N. J. Jeon, J. H. Noh, Y. C. Kim, W. S. Yang, S. Ryu, S. I. Seok, *Nat. Mater.* **2014**, *13*, 897.
[4] W. S. Yang, J. H. Noh, N. J. Jeon, Y. C. Kim, S. Ryu, J. Seo, S. I. Seok, *Science* **2015**, *348*, 1234.
[5] M. Jeong, I. W. Choi, E. M. Go, Y. Cho, M. Kim, B. Lee, S. Jeong, Y. Jo, H. W. Choi, J. Lee, J.-H. Bae, S. K. Kwak, D. S. Kim, C. Yang, *Science* **2020**, *369*, 1615.
[6] M. Kim, J. Jeong, H. Lu, T. K. Lee, F. T. Eickemeyer, Y. Liu, I. W. Choi, S. J. Choi, Y. Jo, H.-B. Kim, S.-I. Mo, Y.-K. Kim, H. Lee, N. G. An, S. Cho, W. R. Tress, S. M. Zakeeruddin, A. Hagfeldt, J. Y. Kim, M. Grätzel, D. S. Kim, *Science* **2022**, *375*, 302.
[7] Best Research-Cell Efficiency Chart, https://www.nrel.gov/pv/cell-efficiency.html (accessed: December 2021).
[8] Q. Han, Y.-T. Hsieh, L. Meng, J.-L. Wu, P. Sun, E.-P. Yao, S.-Y. Chang, S.-H. Bae, T. Kato, V. Bermudez, Y. Yang, *Science* **2018**, *361*, 904.
[9] G. E. Eperon, T. Leijtens, K. A. Bush, R. Prasanna, T. Green, J. T.-W. Wang, D. P. Mcmeekin, G. Volonakis, R. L. Milot, R. May, A. Palmstrom, D. J. Slotcavage, R. A. Belisle, J. B. Patel, E. S. Parrott, R. J. Sutton, W. Ma, F. Moghadam, B. Conings, A. Babayigit, H.-G. Boyen, S. Bent, F. Giustino, L. M. Herz, M. B. Johnston, M. D. Mcgehee, H. J. Snaith, *Science* **2016**, *354*, 861.
[10] O. D. Miller, E. Yablonovitch, S. R. Kurtz, *IEEE J. Photovoltaics* **2012**, *2*, 303.
[11] K. A. Bush, A. F. Palmstrom, Z. J. Yu, M. Boccard, R. Cheacharoen, J. P. Mailoa, D. P. Mcmeekin, R. L. Z. Hoye, C. D. Bailie, T. Leijtens, I. M. Peters, M. C. Minichetti, N. Rolston, R. Prasanna, S. Sofia, D. Harwood, W. Ma, F. Moghadam, H. J. Snaith, T. Buonassisi, Z. C. Holman, S. F. Bent, M. D. Mcgehee, *Nat. Energy* **2017**, *2*, 17009.
[12] Z. Yu, Z. Yang, Z. Ni, Y. Shao, B. Chen, Y. Lin, H. Wei, Z. J. Yu, Z. Holman, J. Huang, *Nat. Energy* **2020**, *5*, 657.
[13] A. Rajagopal, Z. Yang, S. B. Jo, I. L. Braly, P.-W. Liang, H. W. Hillhouse, A. K.-Y. Jen, *Adv. Mater.* **2017**, *29*, 1702140.
[14] T. Leijtens, K. A. Bush, R. Prasanna, M. D. Mcgehee, *Nat. Energy* **2018**, *3*, 828.
[15] N. N. Lal, Y. Dkhissi, W. Li, Q. Hou, Y.-B. Cheng, U. Bach, *Adv. Energy Mater.* **2017**, *7*, 1602761.
[16] K. Xiao, R. Lin, Q. Han, Y. Hou, Z. Qin, H. T. Nguyen, J. Wen, M. Wei, V. Yeddu, M. I. Saidaminov, Y. Gao, X. Luo, Y. Wang, H. Gao, C. Zhang, J. Xu, J. Zhu, E. H. Sargent, H. Tan, *Nat. Energy* **2020**, *5*, 870.
[17] Z. Yang, Z. Yu, H. Wei, X. Xiao, Z. Ni, B. Chen, Y. Deng, S. N. Habisreutinger, X. Chen, K. Wang, J. Zhao, P. N. Rudd, J. J. Berry, M. C. Beard, J. Huang, *Nat. Commun.* **2019**, *10*, 4498.
[18] W. Ke, M. G. Kanatzidis, *Nat. Commun.* **2019**, *10*, 965.
[19] R. Prasanna, T. Leijtens, S. P. Dunfield, J. A. Raiford, E. J. Wolf, S. A. Swifter, J. Werner, G. E. Eperon, C. De Paula, A. F. Palmstrom, C. C. Boyd, M. F. A. M. Van Hest, S. F. Bent, G. Teeter, J. J. Berry, M. D. Mcgehee, *Nat. Energy* **2019**, *4*, 939.
[20] R. Lin, K. Xiao, Z. Qin, Q. Han, C. Zhang, M. Wei, M. I. Saidaminov, Y. Gao, J. Xu, M. Xiao, A. Li, J. Zhu, E. H. Sargent, H. Tan, *Nat. Energy* **2019**, *4*, 864.
[21] T. Shi, H.-S. Zhang, W. Meng, Q. Teng, M. Liu, X. Yang, Y. Yan, H.-L. Yip, Y.-J. Zhao, *J. Mater. Chem. A* **2017**, *5*, 15124.
[22] R. L. Milot, M. T. Klug, C. L. Davies, Z. Wang, H. Kraus, H. J. Snaith, M. B. Johnston, L. M. Herz, *Adv. Mater.* **2018**, *30*, 1804506.
[23] S. Gupta, D. Cahen, G. Hodes, *J. Phys. Chem. C* **2018**, *122*, 13926.
[24] Y. Hu, X. Yao, D. G. Schlom, S. Datta, K. Cho, *Chem. Mater.* **2020**, *33*, 212.
[25] X. Meng, T. Wu, X. Liu, X. He, T. Noda, Y. Wang, H. Segawa, L. Han, *J. Phys. Chem. Lett.* **2020**, *11*, 2965.
[26] Q. Tai, X. Guo, G. Tang, P. You, T.-W. Ng, D. Shen, J. Cao, C.-K. Liu, N. Wang, Y. Zhu, C.-S. Lee, F. Yan, *Angew. Chem., Int. Ed.* **2019**, *58*, 806.
[27] J. Tong, Z. Song, D. H. Kim, X. Chen, C. Chen, A. F. Palmstrom, P. F. Ndione, M. O. Reese, S. P. Dunfield, O. G. Reid, J. Liu, F. Zhang, S. P. Harvey, Z. Li, S. T. Christensen, G. Teeter, D. Zhao, M. M. Al-Jassim, M. F. A. M. Van Hest, M. C. Beard, S. E. Shaheen, J. J. Berry, Y. Yan, K. Zhu, *Science* **2019**, *364*, 475.
[28] M. Wei, K. Xiao, G. Walters, R. Lin, Y. Zhao, M. I. Saidaminov, P. Todorović, A. Johnston, Z. Huang, H. Chen, A. Li, J. Zhu, Z. Yang, Y.-K. Wang, A. H. Proppe, S. O. Kelley, Y. Hou, O. Voznyy, H. Tan, E. H. Sargent, *Adv. Mater.* **2020**, *32*, 1907058.
[29] Z. Ni, C. Bao, Y. Liu, Q. Jiang, W.-Q. Wu, S. Chen, X. Dai, B. Chen, B. Hartweg, Z. Yu, Z. Holman, J. Huang, *Science* **2020**, *367*, 1352.
[30] Q. Jiang, Z. Ni, G. Xu, Y. Lin, P. N. Rudd, R. Xue, Y. Li, Y. Li, Y. Gao, J. Huang, *Adv. Mater.* **2020**, *32*, 2001581.
[31] W.-Q. Wu, P. N. Rudd, Z. Ni, C. H. Van Brackle, H. Wei, Q. Wang, B. R. Ecker, Y. Gao, J. Huang, *J. Am. Chem. Soc.* **2020**, *142*, 3989.
[32] T. Leijtens, R. Prasanna, K. A. Bush, G. E. Eperon, J. A. Raiford, A. Gold-Parker, E. J. Wolf, S. A. Swifter, C. C. Boyd, H.-P. Wang, M. F. Toney, S. F. Bent, M. D. Mcgehee, *Sustainable Energy Fuels* **2018**, *2*, 2450.
[33] R. Lin, J. Xu, M. Wei, Y. Wang, Z. Qin, Z. Liu, J. Wu, K. Xiao, B. Chen, S. M. Park, G. Chen, H. R. Atapattu, K. R. Graham, J. Xu, J. Zhu, L. Li, C. Zhang, E. H. Sargent, H. Tan, *Nature* **2022**, *603*, 73.
[34] M. V. Khenkin, E. A. Katz, A. Abate, G. Bardizza, J. J. Berry, C. Brabec, F. Brunetti, V. Bulović, Q. Burlingame, A. Di Carlo, R. Cheacharoen, Y.-B. Cheng, A. Colsmann, S. Cros, K. Domanski, M. Dusza, C. J. Fell, S. R. Forrest, Y. Galagan, D. Di Girolamo, M. Grätzel, A. Hagfeldt, E. Von Hauff, H. Hoppe, J. Kettle, H. Köbler, M. S. Leite, S. Liu, Y.-L. Loo, J. M. Luther, et al., *Nat. Energy* **2020**, *5*, 35.
[35] X. Chen, K. Wang, M. C. Beard, *Phys. Chem. Chem. Phys.* **2019**, *21*, 16399.
[36] Y. Zhai, K. Wang, F. Zhang, C. Xiao, A. H. Rose, K. Zhu, M. C. Beard, *ACS Energy Lett.* **2020**, *5*, 47.
[37] J. Xue, R. Wang, X. Chen, C. Yao, X. Jin, K.-L. Wang, W. Huang, T. Huang, Y. Zhao, Y. Zhai, D. Meng, S. Tan, R. Liu, Z.-K. Wang, C. Zhu, K. Zhu, M. C. Beard, Y. Yan, Y. Yang, *Science* **2021**, *371*, 636.
[38] N. Phung, R. Félix, D. Meggiolaro, A. Al-Ashouri, G. S. E Silva, C. Hartmann, J. Hidalgo, H. Köbler, E. Mosconi, B. Lai, R. Gunder, M. Li, K.-L. Wang, Z.-K. Wang, K. Nie, E. Handick, R. G. Wilks, J. A. Marquez, B. Rech, T. Unold, J.-P. Correa-Baena, S. Albrecht, F. De Angelis, M. Bär, A. Abate, *J. Am. Chem. Soc.* **2020**, *142*, 2364.
[39] S. Chen, X. Xiao, B. Chen, L. L. Kelly, J. Zhao, Y. Lin, M. F. Toney, J. Huang, *Sci. Adv.* **2021**, *7*, eabb2412.
[40] P. Cui, D. Wei, J. Ji, H. Huang, E. Jia, S. Dou, T. Wang, W. Wang, M. Li, *Nat. Energy* **2019**, *4*, 150.
[41] J. M. Frost, K. T. Butler, F. Brivio, C. H. Hendon, M. Van Schilfgaarde, A. Walsh, *Nano Lett.* **2014**, *14*, 2584.
[42] M. U. Rothmann, W. Li, J. Etheridge, Y.-B. Cheng, *Adv. Energy Mater.* **2017**, *7*, 1700912.
[43] W.-J. Yin, J.-H. Yang, J. Kang, Y. Yan, S.-H. Wei, *J. Mater. Chem. A* **2015**, *3*, 8926.
[44] Y. Yuan, J. Huang, *Acc. Chem. Res.* **2016**, *49*, 286.
[45] H. Yu, H. Lu, F. Xie, S. Zhou, N. Zhao, *Adv. Funct. Mater.* **2016**, *26*, 1411.
[46] C. Li, A. Guerrero, Y. Zhong, A. Gräser, C. A. M. Luna, J. Köhler, J. Bisquert, R. Hildner, S. Huettner, *Small* **2017**, *13*, 1701711.
[47] Y. Fang, Q. Dong, Y. Shao, Y. Yuan, J. Huang, *Nat. Photonics* **2015**, *9*, 679.
[48] Q. Wang, Y. Shao, H. Xie, L. Lyu, X. Liu, Y. Gao, J. Huang, *Appl. Phys. Lett.* **2014**, *105*, 163508.
[49] S. P. Harvey, J. Messinger, K. Zhu, J. M. Luther, J. J. Berry, *Adv. Energy Mater.* **2020**, *10*, 1903674.
[50] J. P. Perdew, K. Burke, M. Ernzerhof, *Phys. Rev. Lett.* **1996**, *77*, 3865.
[51] J. Heyd, G. E. Scuseria, M. Ernzerhof, *J. Chem. Phys.* **2003**, *118*, 8207.
[52] G. Kresse, J. Furthmüller, *Phys. Rev. B* **1996**, *54*, 11169.